ARTICLE

doi:10.1038/nature14427

Structure of the human 80S ribosome

Heena Khatter[1,2,3,4]*, Alexander G. Myasnikov[1,2,3,4]*, S. Kundhavai Natchiar[1,2,3,4]* & Bruno P. Klaholz[1,2,3,4]

Ribosomes are translational machineries that catalyse protein synthesis. Ribosome structures from various species are known at the atomic level, but obtaining the structure of the human ribosome has remained a challenge; efforts to address this would be highly relevant with regard to human diseases. Here we report the near-atomic structure of the human ribosome derived from high-resolution single-particle cryo-electron microscopy and atomic model building. The structure has an average resolution of 3.6 Å, reaching 2.9 Å resolution in the most stable regions. It provides unprecedented insights into ribosomal RNA entities and amino acid side chains, notably of the transfer RNA binding sites and specific molecular interactions with the exit site tRNA. It reveals atomic details of the subunit interface, which is seen to remodel strongly upon rotational movements of the ribosomal subunits. Furthermore, the structure paves the way for analysing antibiotic side effects and diseases associated with deregulated protein synthesis.

Ribosomes form the hub of translation across all kingdoms of life, synthesizing proteins using an mRNA template. An interesting concept that has emerged from previous ribosome structures is its layered evolution, with a conserved core across all species comprising the catalytic peptidyl transferase centre (PTC) and GTPase- (guanosine triphosphatase) associated centre in the large ribosomal subunit, and the decoding centre in the small subunit[1]. The exceptionally complex ribosomes of multicellular eukaryotes contain additional rRNA components, termed expansion segments (ES), and additional protein moieties as compared to their prokaryotic counterparts. The human ribosome (80S) has a molecular weight of 4.3 MDa: the large subunit (60S) consists of 28S, 5S and 5.8S rRNAs and 47 proteins, while the small subunit (40S) possesses a single 18S rRNA chain and 33 proteins. The structures of mammalian cytoplasmic ribosomes have provided locations and folds of all eukaryote-specific components[1–7]. A recent structure of the human ribosome at an average resolution of ~5.4–6.0 Å provided useful insights[1]; however, structural data closer to 3.0 Å resolution are required to derive an atomic model of the human ribosome, the ultimate goal of eukaryotic ribosome structural studies. The ribosome is a target for various human diseases (notably infectious diseases and cancer), which gives a structure at or around 3.0 Å resolution added medical importance, especially with regard to the growing problems of antibiotic resistance and drug therapy side effects.

Over the past year, structure determination of asymmetric objects such as the ribosome by single-particle cryo-electron microscopy (cryo-EM) has reached the 3–4 Å resolution range (for example, refs 8–11), owing largely to improved electron detectors[12–14]. Nevertheless, the potential of cryo-EM-associated atomic model building and refinement procedures as used in the field of X-ray crystallography has not been fully exploited, especially in terms of structure refinement of large macromolecular complexes. Here we present the near-atomic structure of the human ribosome determined using high-resolution electron microscopy and a direct electron detector (complementary metal oxide semiconductor (CMOS) detector with a back-thinned direct detection device (DDD) sensor) in combination with recent developments in image processing (dose fractionation and movie processing), 3D reconstruction and atomic model building using crystallography refinement procedures. The structure of the human 80S ribosome provides unprecedented insights into rRNAs and ribosomal proteins down to the level of individual residue side chains, inter-subunit contacts, functionally relevant key regions including the PTC and the decoding region, interactions with the tRNA present in the exit (E) site, and potential ligand-binding pockets. These can be further exploited for the molecular description of antibiotic and other potential drug pockets.

Structure determination

Human 80S ribosomes from HeLa cells were prepared using a recently established protocol[15] that yields highly homogenous samples of crystallizable quality and which contain a tRNA in the E-site; however, X-ray diffraction of these crystals was limited to ~25 Å (ref. 15). The combination of highly homogenous samples with on-site advanced single-particle cryo-EM imaging techniques (including movie processing done here with only 3 frames) produced a structure at near-atomic resolution (Fig. 1). While the average resolution is estimated to ~3.6 Å (Extended Data Fig. 1), local resolution calculations (Fig. 2) show that most regions are between 2.4 and 4.6 Å resolution, with significant components at 2.9 Å (see features in Extended Data Fig. 2), and only decrease to ~6 Å in the more flexible regions at the periphery. An atomic model of the human ribosome was obtained by extensive model building and restrained parameter refinement protocols[16] (see Methods). We combined this approach with a recent development in the field of X-ray crystallography called feature-enhanced map (FEM[17]), which robustly increases the interpretability of maps. For the first time, FEM map calculations were used in the context of cryo-EM maps for structure interpretation (Fig. 2c, d), which for the well-ordered regions of the human 80S ribosome show resolution and features that go beyond those of the original cryo-EM map. Final electron density maps were calculated by combining phases of the refined atomic model and Fourier coefficients derived from the cryo-EM map, as is routinely done in the crystallography field, yielding further improved maps with features clearly beyond 3 Å resolution (Fig. 2e and Extended Data Figs 3 and 4). This observation indicates that useful amplitudes are present in the cryo-EM data beyond the average resolution estimated by Fourier-shell correlation.

[1]Centre for Integrative Biology (CBI), Department of Integrated Structural Biology, IGBMC (Institute of Genetics and of Molecular and Cellular Biology), 1 rue Laurent Fries, 67404 Illkirch, France. [2]Centre National de la Recherche Scientifique (CNRS), UMR 7104, 67404 Illkirch, France. [3]Institut National de la Santé et de la Recherche Médicale (INSERM) U964, 67404 Illkirch, France. [4]Université de Strasbourg, 67081 Strasbourg, France.
*These authors contributed equally to this work.

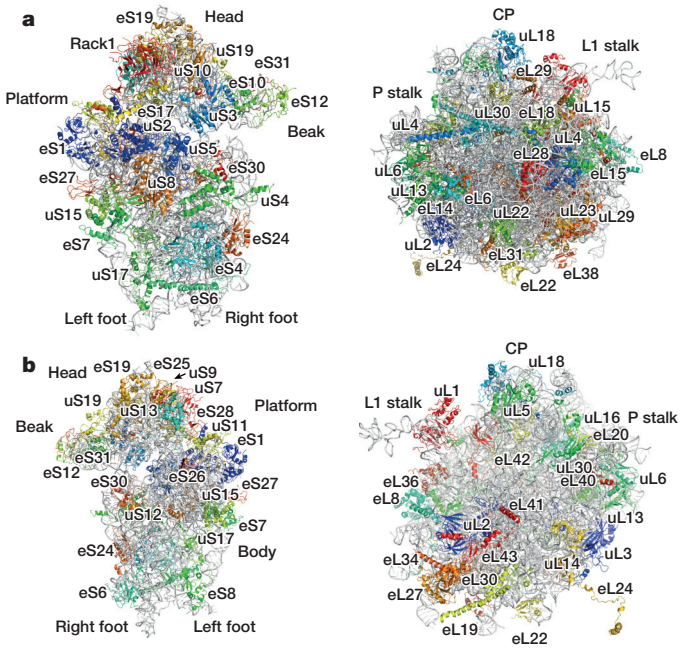

Figure 1 | Overall structure of the human 80S ribosome. **a**, **b**, Global views of the 80S human ribosome from the solvent sides of the 60S and 40S subunits (**a**) and from the inter-subunit interfaces with ribosomal proteins indicated on the atomic model (**b**) (backbone representation; proteins uS14, eS21, eL13, eL21, uL24, eL32, eL33, eL37 and eL39 further inside the structure are not labelled).

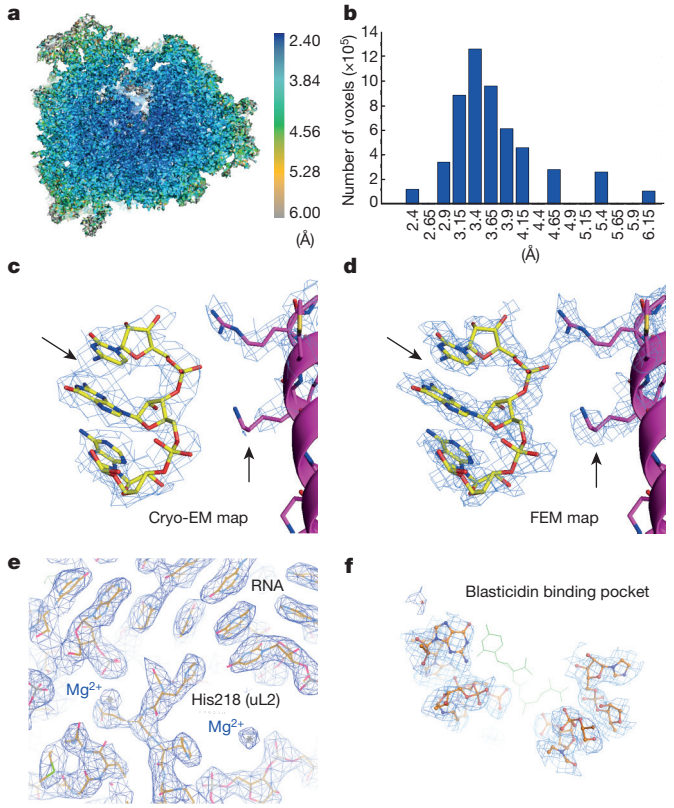

Figure 2 | Local resolution and electron density maps. **a**, **b**, Local resolution estimation of the cryo-EM map (central section) and histogram distribution of resolution values. **c**, **d**, Comparison of cryo-EM (**c**) and FEM (**d**) maps (arrows highlight regions with improved density). **e**, Example of electron density map obtained by combining amplitudes derived from the cryo-EM map and phases calculated from the iteratively refined atomic model (Phenix map calculation), illustrating the interactions of ribosomal protein uL2 with 28S rRNA. **f**, Example of the definition of side-chain residues (Phenix map) forming a ligand-binding pocket (here modelled with blasticidin, a nonspecific antibiotic) as required for structure-guided drug design purposes.

The final atomic model (Fig. 1) comprises ~220,000 atoms across the 5,866 nucleotide residues and ~11,590 amino acids of the 80 proteins, the 4 rRNAs and E-site tRNA, and 239 Mg^{2+} ions.

Description of the overall structure

The overall structure shows the common landmarks of the 40S and 60S ribosomal subunits (Fig. 1). Compared to the yeast ribosome[2,18], the human ribosome contains an additional protein, eL28 (ref. 1). We observed additional densities corresponding to the carboxy terminus of uS2 (residues 209–222) and also redefined the globular structure of protein eS17 (residues 72–93) in the 40S subunit (Extended Data Fig. 5). The present structure represents a pre-translocation state in which the 40S subunit is non-rotated (Fig. 3); this non-ratcheted state is similar to the yeast ribosome[2], while the recent human and porcine ribosome structures exhibit essentially the same post-translocation conformation due to the presence of elongation factor eEF2 (refs 1, 8). The present conformation is consistent with the presence of a tRNA molecule in the E-site and the movement of the L1 stalk towards the core of the ribosome. The L1 stalk rRNA interacts with the tRNA close to the elbow region, as observed earlier for the 70S

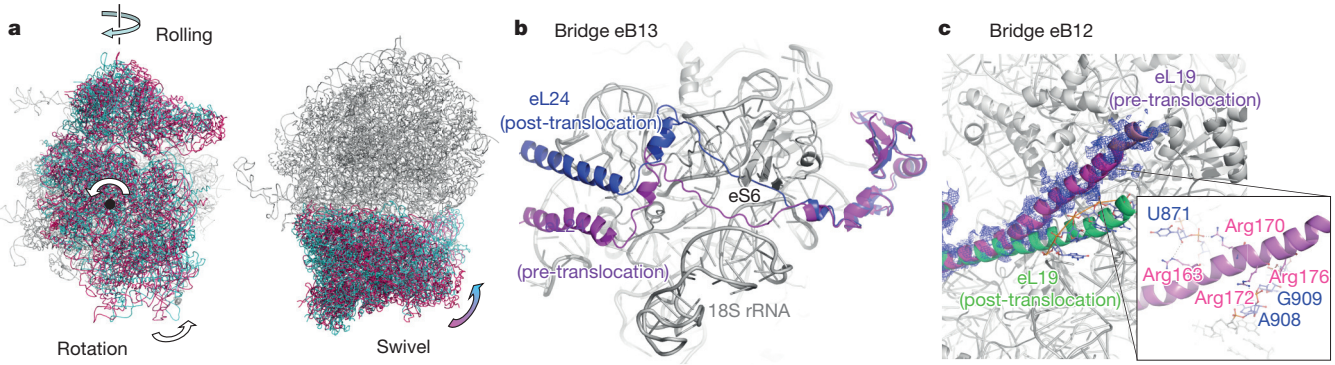

Figure 3 | Conformational changes of the human ribosome. **a**, Comparison of the human ribosome structure in the pre-translocation state (present study, pink 40S, grey 60S) and in the post-translocation state (when factor eEF2 is present, cyan 40S, porcine ribosome), revealing three major types of movement. **b**, **c**, Illustration of large conformational changes of protein eL24 (eB13) and eL19 (eB12) occurring upon 40S subunit rotation. The C-terminal helix of eL24 is relocated to interact with a different region of the 18S rRNA. eL19 undergoes a structural transition from a straight (green, post-translocation state[1,8]) to a bent protein helix (pink, pre-translocation state, present study).

ribosome[19–22]. In contrast to the previous human and porcine ribosome structures, the 40S subunit head shows a swivel movement away from the 60S, which leads to a partial closure of the latch region (Figs 1 and 3a). This could be related with the fact that the mRNA channel is empty, that is, it contains neither mRNA nor protein factors involved in ribosome starvation, in contrast with previous yeast and human ribosome structures[1,2]. In summary, the 40S subunit undergoes three characteristic types of conformational changes: (1) a universal rotation similar to 'ratcheting' in bacterial ribosomes[23]; (2) a swivel movement of the 40S head and beak regions in the direction of the tRNA E-site; and (3) a rotation of the 40S body around a vertical axis perpendicular to the classical rotation axis termed 'subunit rolling' (not observed in bacterial ribosomes, but recently described for a eukaryotic complex[24]; Fig. 3a). The subunit rolling leads to a slight opening of the ribosomal subunit interface (discussed below) on the side of the factor entry site where ribosomal GTPases bind. In this context, it is also interesting to note that relatively large crevasses and gaps exist between the different structural domains of the 18S rRNA, which could serve to accommodate conformational changes of the 40S throughout the translation process.

The transition from a pre- to a post-translocation state induces several major rearrangements in the structure, highlighted by ribosomal proteins eL24 and eL19 (Fig. 3b, c), which constitute some of the characteristic eukaryote-specific bridges (eB12 and eB13, annotated in Fig. 4). The C-terminal part of eL24 relocates entirely and forms a new interaction site on the 40S subunit with ribosomal protein eS6 and 18S rRNA (Fig. 3b). In the case of eL19, a long protein helix protrudes from the 60S subunit to cross over to the 40S subunit. This is one of the rare 60S components (apart from the L1 region) that strongly changes conformation upon subunit rotation. The C-terminal helix of eL19 is kinked in the pre-translocation state (and extends by another seven residues), while it is straight in the post-translocation state (Fig. 3c). This conformational transition results in formation of salt bridges between the positively charged Arg172 and Arg176 side chains of protein eL19 and the phosphate moieties of 18S rRNA nucleotides G909 and G910 (Fig. 3c).

Inter–subunit interface

The present structure highlights some of the characteristic intersubunit contact sites in more detail with respect to the molecular interactions between the rRNA and protein residues involved. The interface comprises a series of contact regions that have been annotated (Fig. 4, summarized in Extended Data Table 1) according to the nomenclature used for inter-subunit bridges of the yeast ribosome[2] (extended by two new bridges eB15 and eB16[1], not seen in the present structure). The core of the contact interface is formed by helix H69 (28S rRNA, A3766 region; 'h' and 'H' are used to number rRNA helices of the small and large subunits, respectively) from the 60S subunit which interacts with helix h44 (18S rRNA, G1849 region; Fig. 4) to form bridges B2a and B2b, close to the universal rotation axis (Fig. 3a) around which the ribosomal subunits rotate forward and backwards during the tRNA translocation process, as seen in prokaryotic and eukaryotic ribosomes[22,23,25,26]. Among the known intersubunit bridges, B7b/c and B8 are not observed in the present human 80S ribosome (not including contact-mediating ions such as Os in the yeast 80S structure or Mg^{2+}), while the bridge eB8 contact is mediated by eS1 and eL8, in contrast with the yeast 80S ribosome[2], where eL43 replaces eL8. Furthermore, there is an additional B2e bridge present as observed previously[24]. It is remarkable that a noticeable gap exists between the 40S and 60S subunits in the region below the factor binding site, which is related possibly with the vertical rotation of the 40S subunit and a slight opening of the interface (Fig. 3a). In contrast to other contact regions, there are only few densities observed in the inter-subunit space, which could be ions such as Mg^{2+}. In general, five contact types are observed: ribose–ribose, ribose–phosphate, ribose–base, protein–base and protein–protein interactions (Fig. 5). Below, we highlight some of the most prominent examples of intersubunit contact regions in the human ribosome.

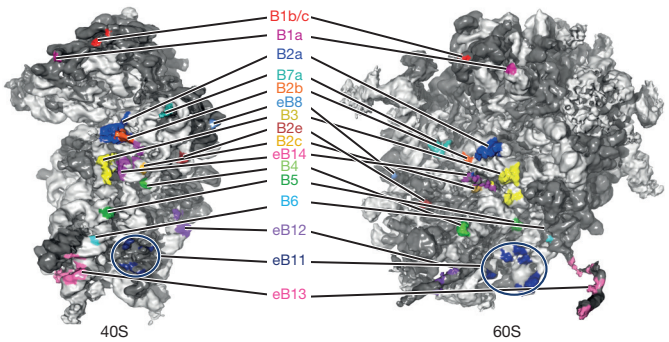

Figure 4 | Ribosomal inter-subunit bridges. Annotation of the inter-subunit bridges at the interface of the 40S and 60S subunits (rRNA in light grey, ribosomal proteins in dark grey, colour-coded bridges are indicated).

A particularly interesting contact type are the interactions mediated by ribose moieties, with the 2′-OH groups of the rRNA backbone sugar moieties playing a key role rather than the charged phosphate groups of the rRNA backbone (Fig. 5a). The 2′-OH groups are offset, leading to a bifurcated hydrogen-bonding pattern. This pattern is distinct from sugar-edge (ribose-base) interactions[27] and somehow similar to that of protein β-sheets involving the carbonyl backbone[28–30]. This leads to a characteristic ribose–ribose interface involving mostly hydroxyl groups of the sugar moieties, as illustrated by the interactions of the 2′-OH groups of nucleotides A1719, A1815 and G1816 (18S rRNA helix h44) with the 2′-OH groups of nucleotides G3806, A3807, C3794 and A3795 (28S rRNA helix H71; Fig. 5a). Similar ribose–ribose interactions exist between ribose moieties in the subunit interface of bacterial ribosomes[31–33]. These ribose–ribose contact regions differ from other regions of the interface in which a significant amount of interactions occur through Mg^{2+}-mediated phosphate–phosphate electrostatic interactions, while the bridges located more at the periphery operate through direct hydrogen bonding rather than being mediated by Mg^{2+} (for example, uS13–uL5, Fig. 5, or the eukaryote-specific eL19 and the 18S rRNA 910 region; Fig. 3b, c). This difference could explain the observation that the biochemical stability of eukaryotic ribosomes is much less Mg^{2+}-dependent as compared to bacterial ribosomes, and much more dependent on K^{+} ions, consistent with the idea that potassium is required for inter-subunit stability while Mg^{2+} ensures proper rRNA folding[15,34–36]. Characteristic protein–RNA interactions exist, for example, between 18S rRNA region 1173 and the amino-terminal helix of protein eL41 and involve phosphate group interactions with positively charged residues (Arg and Lys; Fig. 5b). Other examples of interface remodelling are regions of the ribosomal subunit interface in which rRNA ribose and Mg^{2+}-mediated contacts sites are also seen to switch positions upon rotation of the ribosomal subunits. This involves rearrangement of the interface and Mg^{2+}-ion repositioning (for example, bridges B2b, 1848 nucleotide region of 18S rRNA, and phosphate backbone of nucleotide 1070; solvent channels with residual densities for more potential ions are found right below the E-site tRNA binding site).

Owing to the conformational difference of the structure as compared to previous human and porcine ribosome structures, numerous contact sites are shifted or completely rearranged. Apart from the two examples of bridges eB12 and eB13 described above that involve major conformational changes of the involved proteins, another prominent example is that of bridge B1b/c (Fig. 5c). This contact is located between the central protuberance of the 60S and the 40S head and involves ribosomal proteins uL5 and uS13 (Fig. 5c). Rather than operating through large conformational changes of parts of the

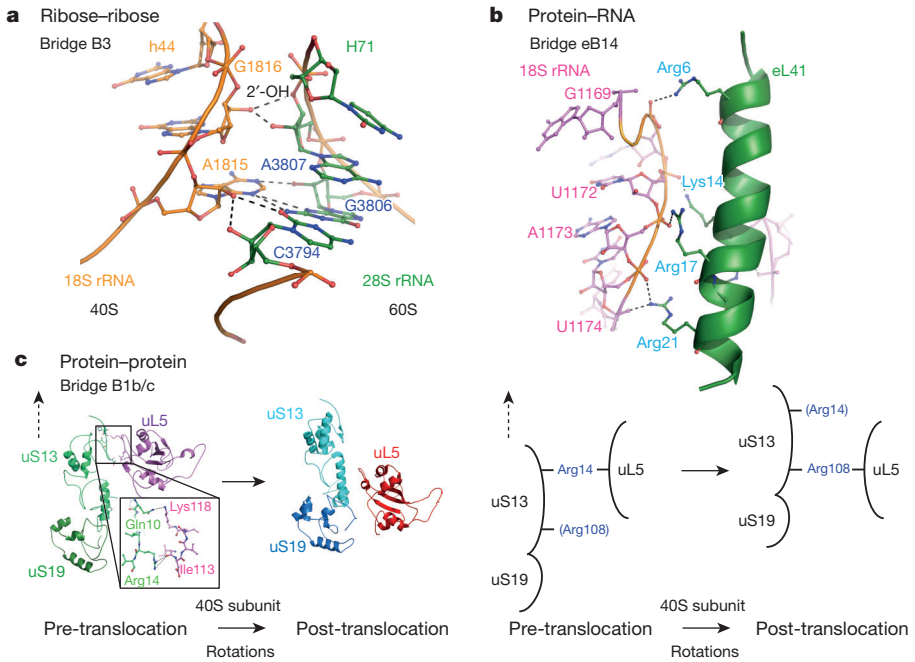

Figure 5 | Molecular details of characteristic inter-subunit contacts. **a**, Detail of bridge B3 highlighting ribose–ribose and ribose–nucleotide interactions between 28S rRNA helix H71 and 18S rRNA helix h44, mediated through the 2′-OH ribose moieties. **b**, Characteristic protein–RNA interaction between 18S rRNA region 1173 and the N-terminal helix of protein eL41 (bridge eB14) involving phosphate group interactions with positively charged residues. **c**, Details of bridge B1b/c which involves proteins uS13 and uL5 close to the central protuberance of the ribosome. The schematic drawing illustrates the remodelling of the inter-subunit interface that occurs at the atomic level between the pre- and post-translocation states (see also Fig. 3; present study and refs. 1, 8, respectively).

proteins, this bridge rearranges through a protein shift that is amplified at the periphery of the 40S subunit when rotating. Upon subunit rotation and 40S head swivelling the molecular interactions between uS13 and uL5 are completely remodelled and the interacting residues of uS13 shift by about 23–26 Å (Cα atom of Arg14 and Arg104, respectively). In the pre-translocation state, Ile113 and Lys118 (uL5) contact the side chains of Arg14 and Gln10 (uS13). By contrast, in the post-translocation state as observed in the previous human and porcine ribosome structures, this bridge is formed by Tyr119 of uL5 with Arg108 of uS13 (see schematic in Fig. 5c); the large shift allows additional interactions between uL5 and uS19 to be formed. Similar rearrangements have been observed in yeast and *Escherichia coli* ribosomes[2,31,37].

tRNA binding sites and molecular recognition in E-site

The present human 80S ribosome contains a co-purified tRNA in the E-site, which is well-defined in the cryo-EM map and appears to stabilize the L1 stalk (Fig. 6a). Comparison with other E-site tRNA structures shows that its conformation is different in the anti-codon loop regions of the decoding stem, while it is similar at the CCA end of the acceptor stem (Fig. 6b). The tRNA is found in the classical E/E state consistent with the pre-translocation state of the ribosome, while it is observed in a P/E hybrid state in the porcine ribosome[8,38,39] (the presence of tRNA at each of these sites is annotated as E/E or P/E, with the first symbol denoting the contact with the small subunit and the second referring to the large subunit). On the 60S subunit, the E-site tRNA interacts with the L1 stalk oriented inwards, and with the L1

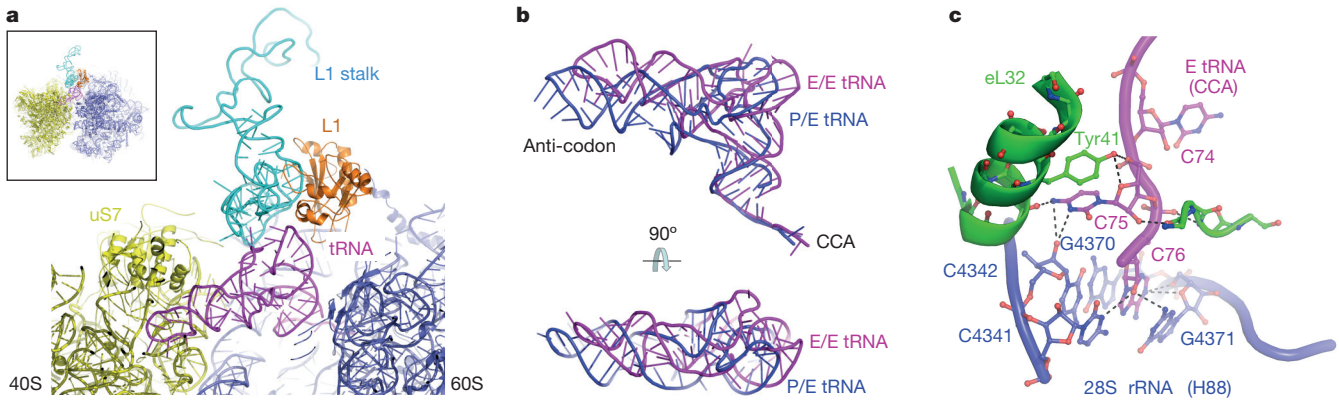

Figure 6 | Molecular recognition by the human ribosome at the level of the E-site tRNA. **a**, Top view of the E-site (ribosomal subunits and the L1 stalk are annotated). **b**, Comparison of the E-site tRNAs from the human and porcine ribosome structures (refs 1, 8; ribosome in the E/E and P/E states, anticodon and CCA regions are labelled). **c**, Details of the interactions between the CCA end region of the E-site tRNA and the 28S rRNA and protein eL32 of the 60S subunit, showing an intercalation of base C76 in between nucleotides G4370 and G4371, and a π-stacking of base C75 with Tyr41 of eL32. The antibiotic cycloheximide would clash with the CCA region of the tRNA.

protein at the level of the tRNA elbow. The L1 stalk rRNA interacts with the tRNA close to the elbow region and at the top of the decoding stem (Fig. 6a). The CCA end exhibits specific interactions in a ligand pocket, formed by G4370 and G4371 of the 28S rRNA and ribosomal protein eL32 (Fig. 6c). A76 of the tRNA intercalates between bases G4370 and G4371, while C75 forms π-stacking interactions with Tyr41 of eL32 (Fig. 6c). The existence of molecular recognition events in the E-site binding pocket is an interesting observation considering that the tRNA behaves as a reaction product, which maintains specific interactions with the enzyme, after the transfer of the nascent peptide to the new P-site tRNA during the translation process. These specific interactions are present although the tRNA probably is a mixture of co-purified tRNAs, suggesting that these interactions are common to all tRNA, consistent with the universal conservation of the CCA end sequence[40]. The binding pocket of the tRNA CCA end overlaps with the binding site of the antibiotic cycloheximide known from the yeast ribosome[41]. On the 40S side, the E-site tRNA decoding stem fits into a pocket formed by protein uS7 and bases G961, A1641 and C1684 of the 18S rRNA (Extended Data Fig. 6). Although details of the ribosome interactions with the anti-codon cannot be resolved, their presence suggests that interactions with the mRNA are partially released in the E-site as seen previously in 70S crystal structures[42].

While the A- and P-sites are empty in the present structure, the two binding pockets are precisely preformed with many structurally well-ordered side chains for molecular recognition of the tRNA molecules. Exceptions to this are A4548 (28S rRNA helix H93, part of the PTC, corresponds to A2602 in *E. coli*) and the central part of protein uL16 that forms a loop (residues 101–117), which are essentially disordered in the P-site (while the C-terminal part of uL16 located in the A-site is fully defined; Extended Data Fig. 6). This suggests that these components of the P-site pocket actively accommodate the tRNA acceptor stem and CCA end upon binding and become structurally ordered (in the presence of a P-site tRNA the loop interacts with bases 1 and 2 of the tRNA)[43].

The structural stabilization upon substrate binding also applies to helix H69 on which the P-site tRNA decoding stem lodges, and to U4452 in the PTC. H69 shows some structural disorder, while 18S rRNA helix h44 with which it forms bridge B2a is well ordered. Thus, P-site tRNA binding is likely to reinforce inter-subunit interactions across this bridge through the stabilization of H69, consistent with the idea that P-site tRNA binding stabilizes the fully assembled 80S complex, which is required for translation initiation[44–46]. Similarly, nucleotide U4452 of 28S rRNA at the entry of the peptide exit channel is disordered in the absence of growing peptide, while all side chains forming the peptide channel through the 60S subunit are well ordered. U4452 is located at a potential branching point of the peptide channel, suggesting that this residue could serve as a gatekeeper to correctly orient the early growing nascent peptide.

Regarding the A-site, all ribosomal residues including nucleotides U4501, U4500 and G4499 (helix H92 of 28S rRNA) are well defined and pre-oriented for base-pair interactions respectively with the complementary C74, C75 and A76 nucleotides of the tRNA, with U4438 (H89 of 28S rRNA) prepared for recognition of A73 of the tRNA. On the 40S subunit, the decoding centre is entirely pre-formed including most side chains. The universally conserved nucleotide residues A1824 and A1825 of 18S rRNA helix h44 (A1492 and A1493 in *E. coli* numbering) are not resolved well enough to designate their position as flipped-in/out, which is known to be important for decoding[47].

Outlook

This work provides, to our knowledge, the first high-resolution structure of the human 80S ribosome with unprecedented insights into rRNA and amino acid residues, including detailed side-chain positions and conformations. It reveals the basis of molecular recognition through hydrogen bonding between ribosomal RNAs and/or protein moieties within the entire ribosome structure, at the level of the exit site tRNA and within the subunit interface, which is seen to remodel upon rotation of the ribosomal subunits. Comparison of the pre- and post-translocation states illustrates how inter-subunit bridges have a marked impact on the dynamics of the human ribosome and provides atomic details about subunit interface rearrangements. While the present ribosome complex contains only an E-site tRNA for which detailed interactions are described here, its structure constitutes a reference for future functional complexes with ribosomal factors such as mRNA, tRNA and associated protein factors, either directly involved in the translation mechanism or implicated in general translation regulation. Biochemically, the present human 80S ribosome samples will be better suited for forming functional complexes because they do not contain any hibernation or starvation factors such as Stm1 (ref. 2) or serpine 1 mRNA-binding protein 1 (SERBP1)[1], located within the path of the mRNA in previous human and yeast ribosome structures.

Another important aspect is that, for drug design purposes, it is crucial to work with the human target rather than with that of related model systems because of unpredictable effects such as second layer residues around ligand-binding pockets, which can modify the interaction pattern of the primary contacting residues or open new pockets by conformational changes of side chains. Our structure provides a valuable repertoire and molecular description of antibiotic binding pockets (Fig. 2f) and other new potentially druggable ligand-binding pockets, which can serve as a basis for structure-guided computer-assisted drug design, *in silico* screening and structure determination of complexes with pharmaceutically relevant ligands. In this respect, we foresee two major applications: (1) reducing side effects of current antibiotics by improving drug specificity; and (2) developing new anticancer agents that target the human ribosome to specifically reduce the elevated protein synthesis rate of cancer cells that makes them a primary target over normally growing cells. The present high-resolution human ribosome structure will hopefully provide new opportunities in drug developments directly relevant for human health.

Online Content Methods, along with any additional Extended Data display items and Source Data, are available in the online version of the paper; references unique to these sections appear only in the online paper.

Received 6 January; accepted 26 March 2015.
Published online 22 April 2015.

1. Anger, A. M. *et al.* Structures of the human and *Drosophila* 80S ribosome. *Nature* **497,** 80–85 (2013).
2. Ben-Shem, A. *et al.* The structure of the eukaryotic ribosome at 3.0 Å resolution. *Science* **334,** 1524–1529 (2011).
3. Rabl, J., Leibundgut, M., Ataide, S. F., Haag, A. & Ban, N. Crystal structure of the eukaryotic 40S ribosomal subunit in complex with initiation factor 1. *Science* **331,** 730–736 (2011).
4. Klinge, S., Voigts-Hoffmann, F., Leibundgut, M., Arpagaus, S. & Ban, N. Crystal structure of the eukaryotic 60S ribosomal subunit in complex with initiation factor 6. *Science* **334,** 941–948 (2011).
5. Spahn, C. M. *et al.* Cryo-EM visualization of a viral internal ribosome entry site bound to human ribosomes: the IRES functions as an RNA-based translation factor. *Cell* **118,** 465–475 (2004).
6. Boehringer, D., Thermann, R., Ostareck-Lederer, A., Lewis, J. D. & Stark, H. Structure of the hepatitis C virus IRES bound to the human 80S ribosome: remodeling of the HCV IRES. *Structure* **13,** 1695–1706 (2005).
7. Chandramouli, P. *et al.* Structure of the mammalian 80S ribosome at 8.7 Å resolution. *Structure* **16,** 535–548 (2008).
8. Voorhees, R. M., Fernandez, I. S., Scheres, S. H. & Hegde, R. S. Structure of the mammalian ribosome-Sec61 complex to 3.4 Å resolution. *Cell* **157,** 1632–1643 (2014).
9. Amunts, A. *et al.* Structure of the yeast mitochondrial large ribosomal subunit. *Science* **343,** 1485–1489 (2014).
10. Greber, B. J. *et al.* The complete structure of the large subunit of the mammalian mitochondrial ribosome. *Nature* **515,** 283–286 (2014).
11. Brown, A. *et al.* Structure of the large ribosomal subunit from human mitochondria. *Science* **346,** 718–722 (2014).
12. Li, X., Zheng, S. Q., Egami, K., Agard, D. A. & Cheng, Y. Influence of electron dose rate on electron counting images recorded with the K2 camera. *J. Struct. Biol.* **184,** 251–260 (2013).
13. Li, X. *et al.* Electron counting and beam-induced motion correction enable near-atomic-resolution single-particle cryo-EM. *Nature Methods* **10,** 584–590 (2013).

14. Bai, X. C., Fernandez, I. S., McMullan, G. & Scheres, S. H. Ribosome structures to near-atomic resolution from thirty thousand cryo-EM particles. *eLife* **2,** e00461 (2013).
15. Khatter, H. *et al.* Purification, characterization and crystallization of the human 80S ribosome. *Nucleic Acids Res.* **42,** e49 (2014).
16. DeLaBarre, B. & Brunger, A. T. Considerations for the refinement of low-resolution crystal structures. *Acta Crystallogr. D* **62,** 923–932 (2006).
17. Afonine, P. V. *et al.* FEM: feature-enhanced map. *Acta Crystallogr. D* **71,** 646–666 (2015).
18. Ben-Shem, A., Jenner, L., Yusupova, G. & Yusupov, M. Crystal structure of the eukaryotic ribosome. *Science* **330,** 1203–1209 (2010).
19. Fei, J., Kosuri, P., MacDougall, D. D. & Gonzalez, R. L. Jr. Coupling of ribosomal L1 stalk and tRNA dynamics during translation elongation. *Mol. Cell* **30,** 348–359 (2008).
20. Cornish, P. V. *et al.* Following movement of the L1 stalk between three functional states in single ribosomes. *Proc. Natl Acad. Sci. USA* **106,** 2571–2576 (2009).
21. Feng, S., Chen, Y. & Gao, Y. G. Crystal structure of 70S ribosome with both cognate tRNAs in the E and P sites representing an authentic elongation complex. *PLoS ONE* **8,** e58829 (2013).
22. Valle, M. *et al.* Locking and unlocking of ribosomal motions. *Cell* **114,** 123–134 (2003).
23. Frank, J. & Agrawal, R. K. A ratchet-like inter-subunit reorganization of the ribosome during translocation. *Nature* **406,** 318–322 (2000).
24. Budkevich, T. V. *et al.* Regulation of the mammalian elongation cycle by subunit rolling: a eukaryotic-specific ribosome rearrangement. *Cell* **158,** 121–131 (2014).
25. Budkevich, T. *et al.* Structure and dynamics of the mammalian ribosomal pretranslocation complex. *Mol. Cell* **44,** 214–224 (2011).
26. Chen, J., Petrov, A., Tsai, A., O'Leary, S. E. & Puglisi, J. D. Coordinated conformational and compositional dynamics drive ribosome translocation. *Nature Struct. Mol. Biol.* **20,** 718–727 (2013).
27. Leontis, N. B. & Westhof, E. Geometric nomenclature and classification of RNA base pairs. *RNA* **7,** 499–512 (2001).
28. Klaholz, B. & Moras, D. C.-H. O hydrogen bonds in the nuclear receptor RARgamma–a potential tool for drug selectivity. *Structure* **10,** 1197–1204 (2002).
29. Liu, A. *et al.* NMR detection of bifurcated hydrogen bonds in large proteins. *J. Am. Chem. Soc.* **130,** 2428–2429 (2008).
30. Jiang, L. & Lai, L. C. H. O hydrogen bonds at protein-protein interfaces. *J. Biol. Chem.* **277,** 37732–37740 (2002).
31. Schuwirth, B. S. *et al.* Structures of the bacterial ribosome at 3.5 Å resolution. *Science* **310,** 827–834 (2005).
32. Cate, J. H., Yusupov, M. M., Yusupova, G. Z., Earnest, T. N. & Noller, H. F. X-ray crystal structures of 70S ribosome functional complexes. *Science* **285,** 2095–2104 (1999).
33. Yusupov, M. M. *et al.* Crystal structure of the ribosome at 5.5 Å resolution. *Science* **292,** 883–896 (2001).
34. Shenvi, C. L., Dong, K. C., Friedman, E. M., Hanson, J. A. & Cate, J. H. Accessibility of 18S rRNA in human 40S subunits and 80S ribosomes at physiological magnesium ion concentrations–implications for the study of ribosome dynamics. *RNA* **11,** 1898–1908 (2005).
35. Moore, M. N. & Spremulli, L. L. Effects of cations and cosolvents on eukaryotic ribosomal subunit conformation. *Biochemistry* **24,** 191–196 (1985).
36. Sperrazza, J. M., Russell, D. W. & Spremulli, L. L. Reversible dissociation of wheat germ ribosomal subunits: cation-dependent equilibria and thermodynamic parameters. *Biochemistry* **19,** 1053–1058 (1980).
37. Zhang, W., Dunkle, J. A. & Cate, J. H. Structures of the ribosome in intermediate states of ratcheting. *Science* **325,** 1014–1017 (2009).
38. Dunkle, J. A. *et al.* Structures of the bacterial ribosome in classical and hybrid states of tRNA binding. *Science* **332,** 981–984 (2011).
39. Tourigny, D. S., Fernandez, I. S., Kelley, A. C. & Ramakrishnan, V. Elongation factor G bound to the ribosome in an intermediate state of translocation. *Science* **340,** 1235490 (2013).
40. Selmer, M. *et al.* Structure of the 70S ribosome complexed with mRNA and tRNA. *Science* **313,** 1935–1942 (2006).
41. Garreau de Loubresse, N. *et al.* Structural basis for the inhibition of the eukaryotic ribosome. *Nature* **513,** 517–522 (2014).
42. Jenner, L., Rees, B., Yusupov, M. & Yusupova, G. Messenger RNA conformations in the ribosomal E site revealed by X-ray crystallography. *EMBO Rep.* **8,** 846–850 (2007).
43. Rhodin, M. H. & Dinman, J. D. A flexible loop in yeast ribosomal protein L11 coordinates P-site tRNA binding. *Nucleic Acids Res.* **38,** 8377–8389 (2010).
44. Yamamoto, H. *et al.* Structure of the mammalian 80S initiation complex with initiation factor 5B on HCV-IRES RNA. *Nature Struct. Mol. Biol.* **21,** 721–727 (2014).
45. Hinnebusch, A. G. The scanning mechanism of eukaryotic translation initiation. *Annu. Rev. Biochem.* **83,** 779–812 (2014).
46. Pestova, T. V. *et al.* Molecular mechanisms of translation initiation in eukaryotes. *Proc. Natl Acad. Sci. USA* **98,** 7029–7036 (2001).
47. Demeshkina, N., Jenner, L., Westhof, E., Yusupov, M. & Yusupova, G. A new understanding of the decoding principle on the ribosome. *Nature* **484,** 256–259 (2012).

Acknowledgements We thank A. Urzhumtsev and P. Afonine for discussions on FEM maps; R. Fritz and J. Michalon for IT support; R. Drui for constant high-quality engineers support; J.-F. Ménétret for technical support; H. Stark for discussions on Cs-correction; D. Moras and J.-C. Thierry for continuous encouragement in pushing structural biology frontiers; the IGBMC cell culture facilities for HeLa cell production; and the High Performance Computing Center of the University of Strasbourg funded by the Equipex Equip@Meso project. This long-term project (since 2003) was supported by the CNRS and the European Research Council (ERC Starting Grant N_243296 TRANSLATIONMACHINERY), and the electron microscope facility was supported by the Alsace Region, the FRM, the IBiSA platform program, INSERM, CNRS and the Association pour la Recherche sur le Cancer (ARC) and by the French Infrastructure for Integrated Structural Biology (FRISBI) ANR-10-INSB-05-01, and Instruct as part of the European Strategy Forum on Research Infrastructures (ESFRI).

Author Contributions H.K. conducted purification, optimization of samples for cryo-EM and cryo-EM data processing. A.G.M. performed cryo-EM data acquisition, image processing, structure refinement and model building. S.K.N. performed structure refinement and model building. B.P.K supervised the study. All authors analysed the data. B.P.K and H.K. wrote the manuscript, with input from A.G.M. and S.K.N.

Author Information The cryo-EM map and atomic coordinates have been deposited in the EMDB and Protein Data Bank under accession codes EMD-2938 and 4ug0, respectively. Reprints and permissions information is available at www.nature.com/reprints. The authors declare no competing financial interests. Readers are welcome to comment on the online version of the paper. Correspondence and requests for materials should be addressed to B.P.K. (klaholz@igbmc.fr).

METHODS

No statistical methods were used to predetermine sample size.

Purification. Human 80S ribosomes were prepared from HeLa cells, purified to homogeneity and characterized biochemically as described earlier[15]. Briefly, the HeLa cells were lysed and the cytosolic extract was then loaded onto 30% sucrose cushion for overnight centrifugation. The ribosomal pellet was treated with puromycin before the final step of sucrose gradient and PEG precipitation. Concentration of purified 80S was calculated using 1 A260 unit corresponds to 20 pmol of 80S ribosome.

Data collection. Freshly prepared human 80S ribosomes (2.5 µl of a 0.5 mg/ml solution) were applied to 300 mesh holey carbon Quantifoil 2/2 grids (Quantifoil Micro Tools, Jena, Germany), blotted with filter paper from both sides in the temperature- and humidity-controlled Vitrobot Mark IV apparatus (FEI, Eindhoven, Netherlands, T = 20 °C, humidity 95%, blot force 5, blot time 0.5 s) and vitrified in liquid ethane pre-cooled by liquid nitrogen. Data were collected on the in-house spherical aberration (Cs) corrected Titan Krios S-FEG instrument (FEI, Eindhoven, Netherlands) operating at 300 kV acceleration voltage and at a nominal underfocus of $\Delta z = -0.6$ to -4.5 µm using the second-generation back-thinned direct electron detector CMOS (Falcon II) 4,096 × 4,096 camera and automated data collection with EPU software (FEI, Eindhoven, Netherlands). The microscope was carefully aligned as well as the Cs corrector. The Falcon II camera was calibrated at nominal magnification of 59,000×. The calibrated magnification on the 14 µm pixel camera was 127,272× resulting in 1.1 Å pixel size at the specimen level. The camera was set up to collect 3 frames (start from the second one) out of 17 possible, plus one total exposure image. Total exposure time was 1 s with a dose of 60 $\bar{e}$ Å^{-2} (or 3.5 $\bar{e}$ Å^{-2} per frame) (where $\bar{e}$ specifies electrons).

Image processing. Before particle picking, stack alignment was performed, which included three frames and total exposure image (total four images in the stack). These four images in the stack were aligned by the whole image motion correction method[13]. Thereafter, an average image of whole stack was used to pick 75,000 particles semi automatically using EMAN2 Boxer[48], and the contrast transfer function of every image was determined using CTFFIND3[49] in the RELION workflow[50]. 2D classification was used to remove bad particles (18,500) and particle sorting was done by 3D classification using 6 classes starting from 56,500 particles, resulting in two dominant classes with 10,000 and 45,000 particles in rotated and non-rotated ribosome conformations, respectively (Extended Data Fig. 7); the subpopulation of the rotated ribosome contains elongation factor eEF2 and the ribosome is in a conformation similar to that of the previous lower-resolution human ribosome structure[1]. For the first steps of refinement, images were coarsened by 2 (C2-images) and 4 (C4-images) using RELION. The initial 2D classification was done with the C4 images, followed by splitting of the different states of the ribosomes using C2 images. Only once the states were clearly separated, uncoarsened (C1) data was used. During the last step of refinement, only close to focus data up to defocus −1.4 µm (about 24,000 particles) was used. At the very last step, the 'movie processing' procedure as implemented in RELION 1.3 version was used with the 3 frames included in the calculations as individual frames. A post-processing procedure implemented in RELION 1.2 (ref. 50) was applied to the final maps for appropriate masking, B-factor sharpening and resolution validation to avoid over-fitting[51]. In this procedure, the appropriate B-factor was determined according to ref. 52. The resolution was estimated in RELION[50], according to the 'gold standard' Fourier shell correlation (FSC = 0.143)[52,53] (Extended Data Fig. 1), indicating an average resolution of 3.6 Å. After calculating local resolution values with ResMap[54] some regions are shown to reach ~2.4 Å resolution in the best cases, and up to 6 Å in the more flexible regions. In general, the 40S subunit appears more flexible resulting in some less well-defined regions at lower resolution as compared to the core of the 60S subunit, which is structurally more stable with the exception of the ES, L1 and P-stalk regions. Map interpretation was done using Chimera[55] and COOT[56] starting from the available atomic models[1,8]. For this, starting atomic models of human and porcine ribosomes[1,8] were placed as individual subunits, rebuilt and the RNA and protein sequences modified according to the human gene sequence. Most ribosomal proteins have about 95–100% conserved sequences in mammals except eL43, eL29, uL29, eL14 and eL6, which were rebuilt with the human sequences (ribosomal proteins follow the new nomenclature[57]). The atomic model was refined against the experimental map using Phenix[58], which included real space refinement, positional refinement, grouped B-factor refinement and simulated annealing. FEM maps were used for structure interpretation and fine-tuning the positions of side-chain conformations throughout the entire structure by manual model building, followed by simulated annealing protocols. We monitored the refinement process with R-factor values to avoid over-fitting, and refined the entire 80S structure at once (to ensure proper distance restraints between residues throughout the structure, notably at the subunit interface) by simulated annealing using parallel computing, rather than refining each protein subunit individually as for the recent porcine ribosome structure[8]. The R-factor value of the refined structure (35.7%) compares well with that of crystal structures[58] showing that the atomic model is well refined compared to crystallography standards. The final atomic model comprises ~220,000 atoms (excluding hydrogens) across the 5,866 nucleotide residues and ~11,590 amino acids of the 80 proteins and the 4 rRNAs (28S, 5S, 5.8S and 18S; excluding certain expansion segment rRNA which are only partially visible at the periphery of the structure probably due to conformational heterogeneity) and 239 Mg^{2+} ions. The structure extends the completeness of the recent porcine ribosome structure at the level of several regions, such as the position of some rRNA segments (however, most rRNA expansion segments remained poorly defined). This includes the region of the L1 rRNA stalk and the L1 protein that could be completed; albeit at lower local resolution, this region is rather well ordered due to the presence of a tRNA in the E-site, which was fully built in the atomic model. Side chains in various sites and pockets are largely well defined (for example, tRNA sites, PTC, decoding site, peptide channel, mRNA channel), unless they become ordered upon substrate binding (see main text); interestingly, the α-sarcin-ricin loop region (rRNA helix H91) is entirely ordered even in the absence of ribosomal GTPases (including the A4605 region, which is catalytically relevant for GTPase activation and the non base-paired G4600 located next to the G-domain of factors). Protein residues of the final atomic model show well-refined geometrical parameters (allowed regions 22.5%, preferred regions 67.9% and 9.5% of outliers in Ramachandran plots, r.m.s. bond deviations of 0.008Å and angle deviations of 1.24°, which compare well with values observed for refined crystal structures). Figures were prepared using the software Chimera[55] and Pymol[60].

48. Ludtke, S. J., Baldwin, P. R. & Chiu, W. EMAN: semiautomated software for high-resolution single-particle reconstructions. *J. Struct. Biol.* **128,** 82–97 (1999).
49. Mindell, J. A. & Grigorieff, N. Accurate determination of local defocus and specimen tilt in electron microscopy. *J. Struct. Biol.* **142,** 334–347 (2003).
50. Scheres, S. H. RELION: implementation of a Bayesian approach to cryo-EM structure determination. *J. Struct. Biol.* **180,** 519–530 (2012).
51. Chen, S. *et al.* High-resolution noise substitution to measure overfitting and validate resolution in 3D structure determination by single particle electron cryomicroscopy. *Ultramicroscopy* **135,** 24–35 (2013).
52. Rosenthal, P. B. & Henderson, R. Optimal determination of particle orientation, absolute hand, and contrast loss in single-particle electron cryomicroscopy. *J. Mol. Biol.* **333,** 721–745 (2003).
53. van Heel, M. & Schatz, M. Fourier shell correlation threshold criteria. *J. Struct. Biol.* **151,** 250–262 (2005).
54. Kucukelbir, A., Sigworth, F. J. & Tagare, H. D. Quantifying the local resolution of cryo-EM density maps. *Nature Methods* **11,** 63–65 (2014).
55. Pettersen, E. F. *et al.* UCSF Chimera–a visualization system for exploratory research and analysis. *J. Comput. Chem.* **25,** 1605–1612 (2004).
56. Emsley, P., Lohkamp, B., Scott, W. G. & Cowtan, K. Features and development of Coot. *Acta Crystallogr. D* **66,** 486–501 (2010).
57. Ban, N. *et al.* A new system for naming ribosomal proteins. *Curr. Opin. Struct. Biol.* **24,** 165–169 (2014).
58. Afonine, P. V. *et al.* Towards automated crystallographic structure refinement with phenix.refine. *Acta Crystallogr. D* **68,** 352–367 (2012).
59. Selmer, M. *et al.* Structure of the 70S ribosome complexed with mRNA and tRNA. *Science* **313,** 1935–1942 (2006).
60. DeLano, W. L. The PyMOL Molecular Graphic System. (DeLano Scientiic, 2002).

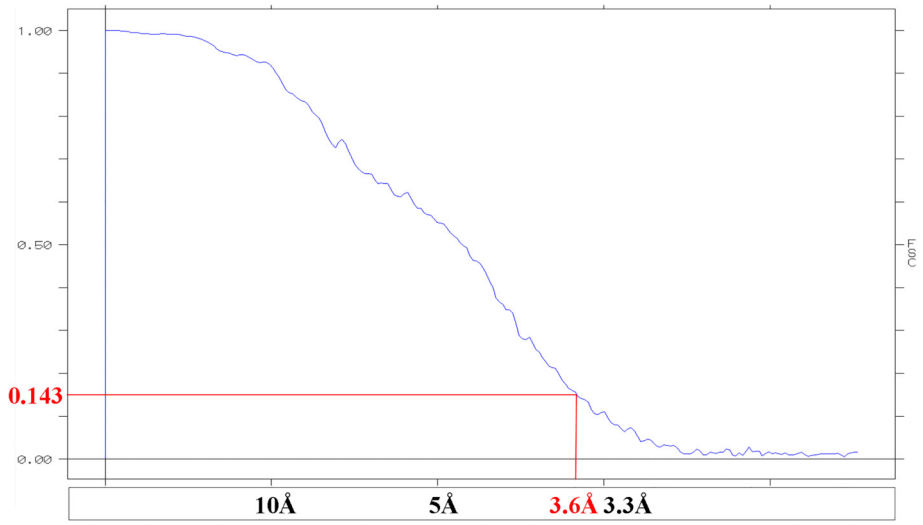

Extended Data Figure 1 | Resolution estimation. The average resolution of the cryo-EM map as estimated from Fourier shell correlation according to the 0.143 criterion.

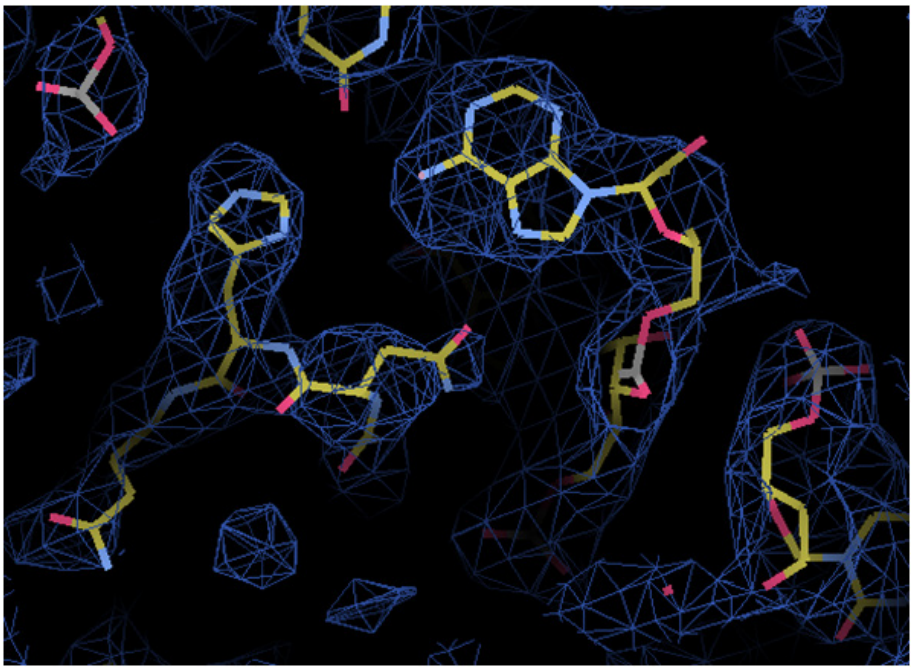

Extended Data Figure 2 | Features of the refined cryo-EM 3D reconstruction. Final cryo-EM map of the peptidyl-transferase centre region illustrating the high level of details observed.

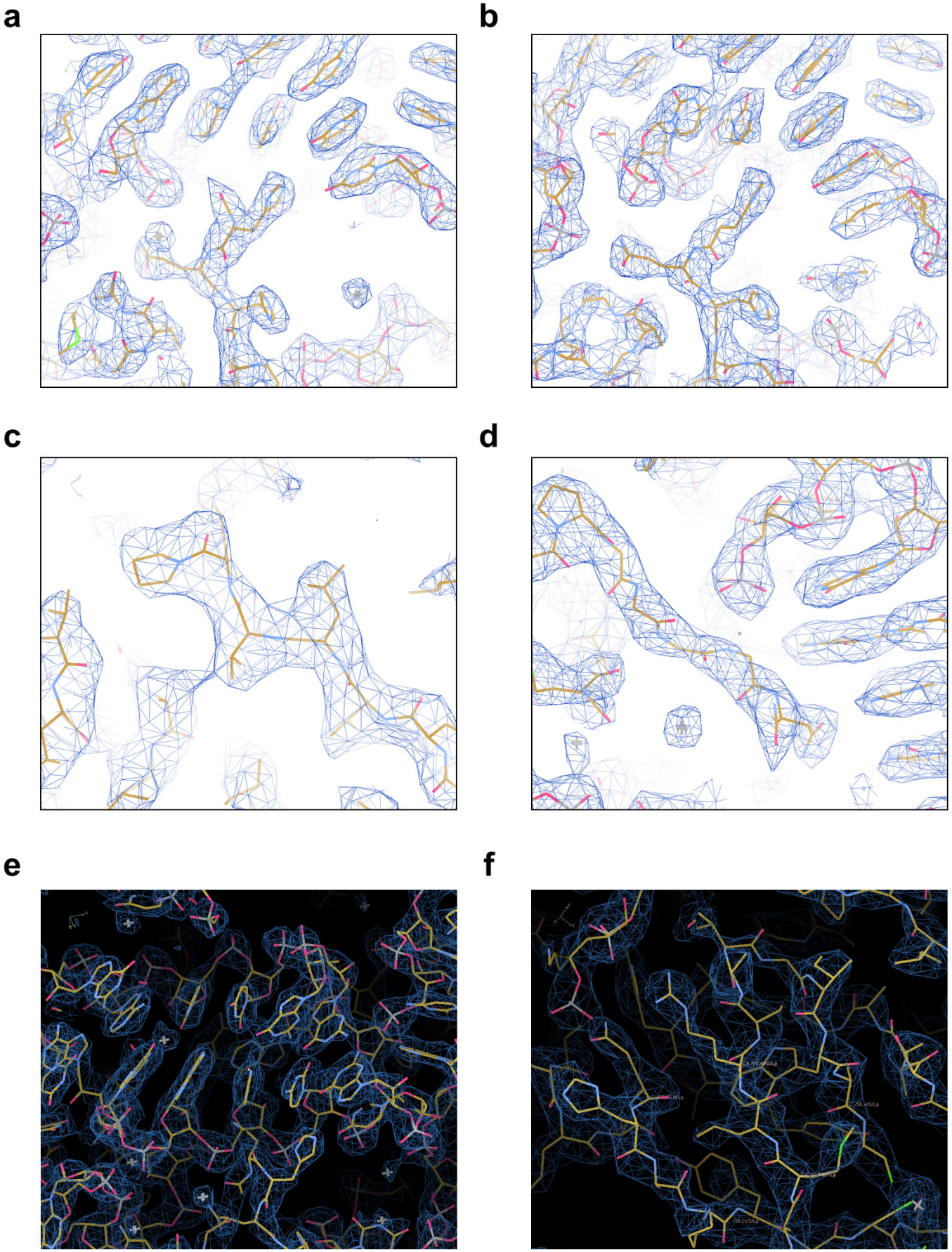

Extended Data Figure 3 | Typical electron density map regions of the human ribosome structure. These final electron density maps were obtained by combining experimental amplitudes derived from the cryo-EM map and phases calculated from the iteratively refined atomic model, as done in standard refinement procedures in X-ray crystallography (see main text).

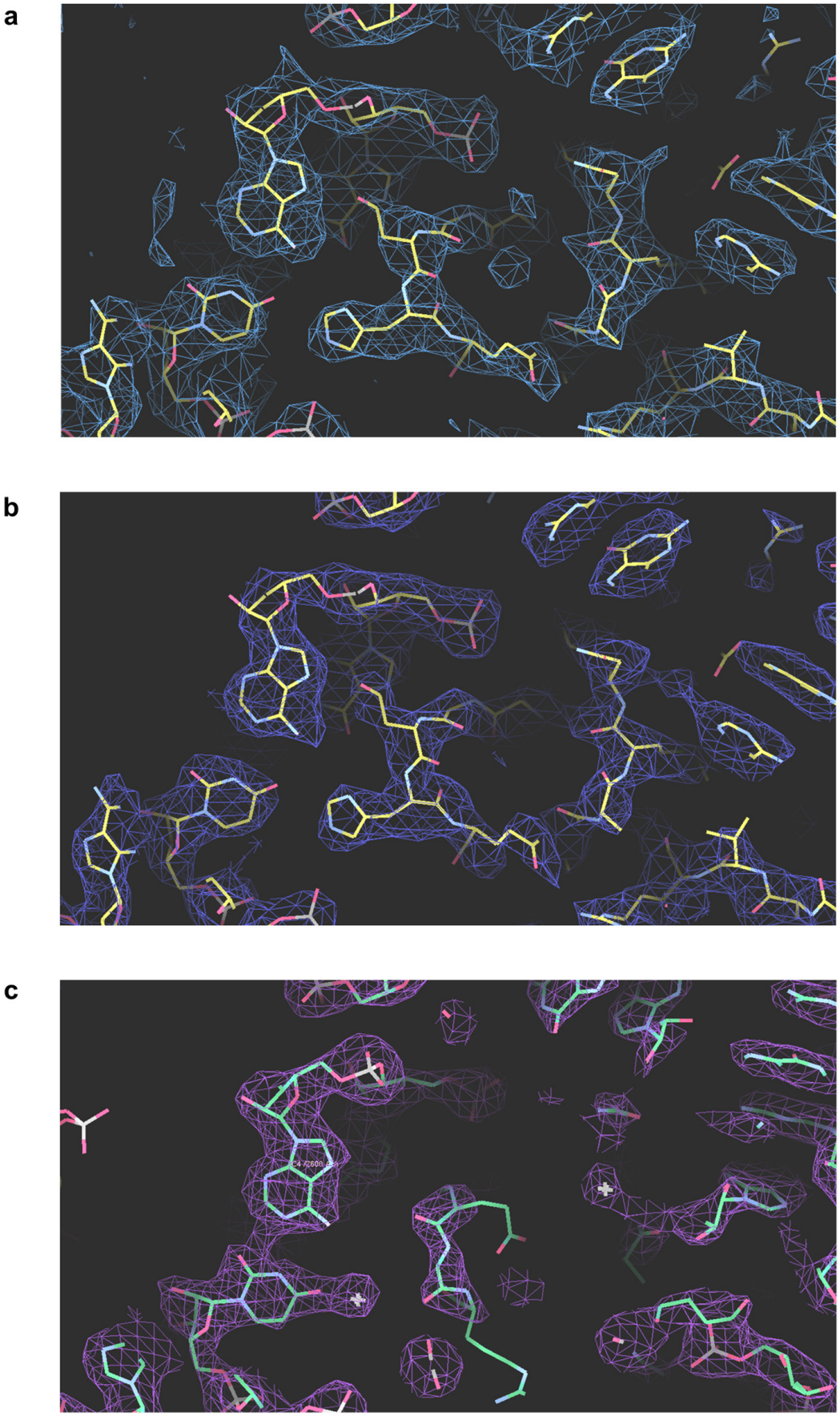

Extended Data Figure 4 | Comparison of maps determined by cryo-EM and X-ray crystallography. Top and middle, cryo-EM map and Phenix map of the human 80S ribosome (this study, A4546 region); bottom, crystal structure of a 70S ribosome at 2.8 Å resolution[59] (corresponding A2600 region).

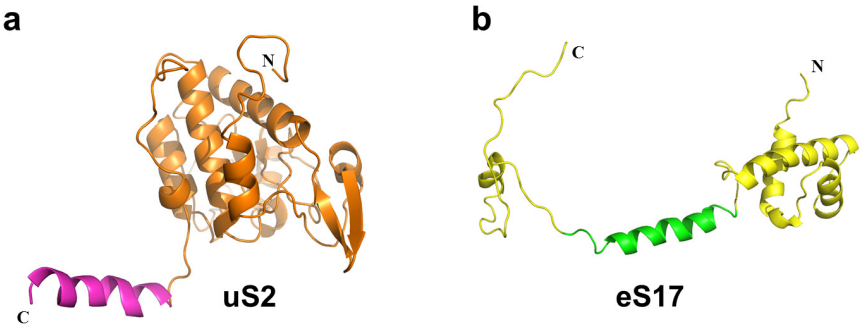

Extended Data Figure 5 | Ribosomal protein structures. **a**, **b**, Structure of ribosomal proteins uS2 and eS17.

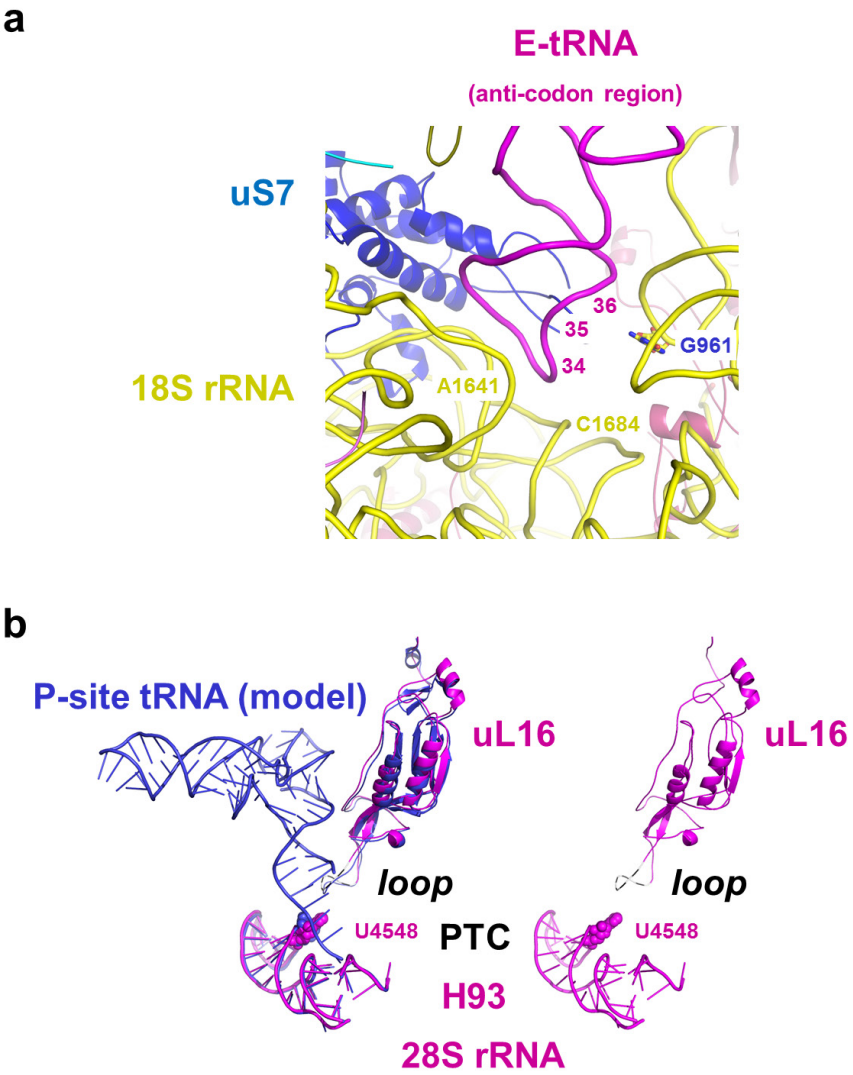

Extended Data Figure 6 | The decoding centre on the 40S. **a**, Contact regions of the E-site tRNA on the 40S subunit. **b**, Catalytic PTC region of the ribosome, highlighting the partial structural disorder of a region of protein uL16 (loop), and disorder of residue U4548 (28S rRNA) in the absence of P-site tRNA, while all other residues are well-ordered. This suggests that the P-site pocket is largely pre-defined while U4548 and the loop participate in tRNA accommodation.

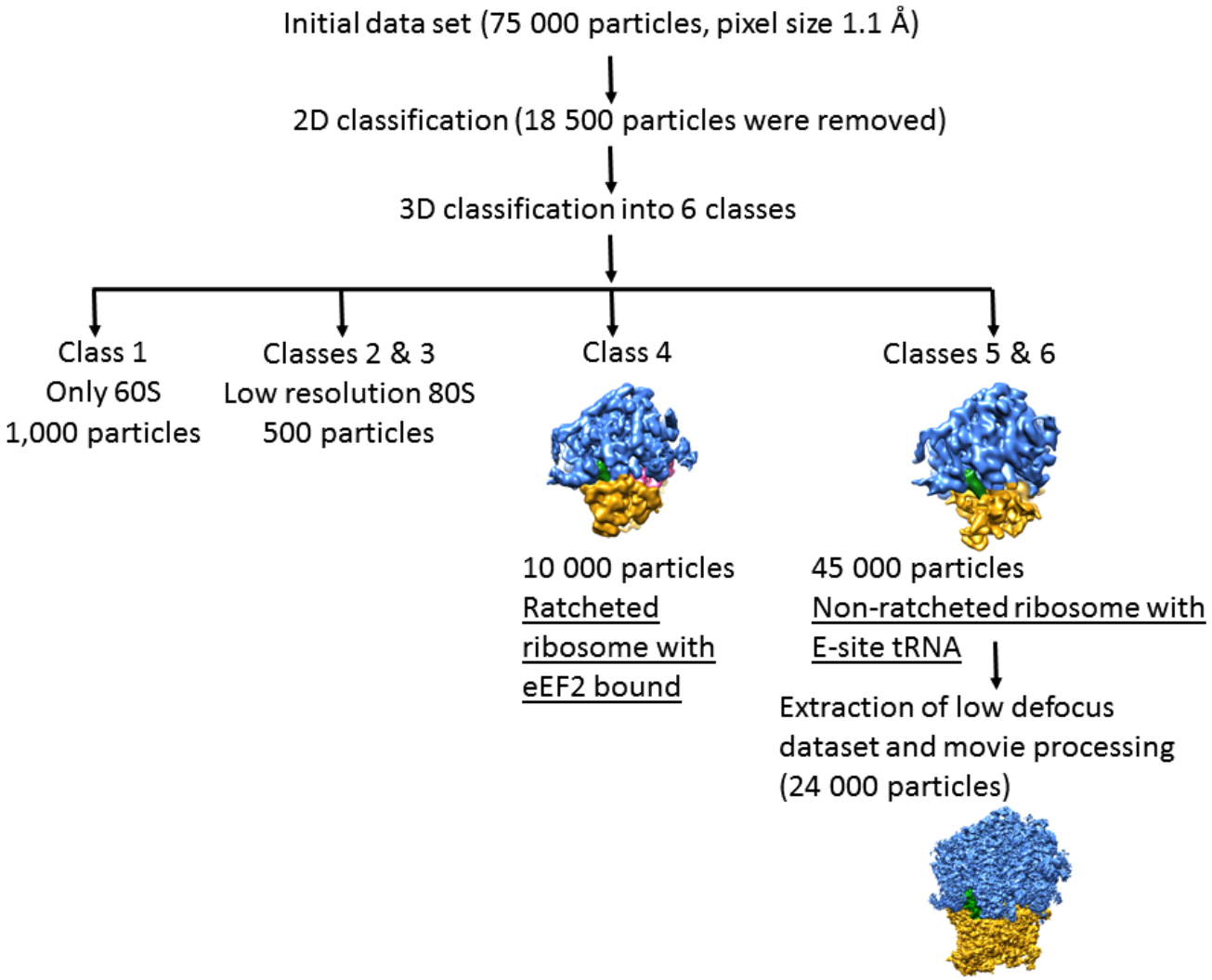

Extended Data Figure 7 | Particle sorting scheme. Particle sorting was done by 3D classification using six classes starting from 75,000 particles, resulting in two dominant classes with 10,000 and 45,000 particles, in rotated and non-rotated ribosome conformations respectively; the highest-resolution close-to-focus data set was refined using movie processing (see Methods).

Extended Data Table 1 | Inter-subunit bridges and 60S and 40S residues involved in inter-subunit interactions

	40S subunit		60S subunit	
B1a	uS19	Arg 10	28S	1766
B1b/c	uS13	Gln 10 Arg 14	uL5	Ile 113 Lys 118
B2a	18S	1707-1709 1826-1829 1849-1850 1059 -1058	28S	3765-3768 3759-3760 3762
B2b	18S	1051	28S	3699
B2c	18S	1180	28S	3694-3695
B2e	18S	938-939	eL43	Arg 85
B3	18S	1815-1819 1719-1721	28S	3805-3807 3794-3796 3628-3629 3834
			eL41	Arg 17 Met 20
B4	18S	1028-1029 677-678	28S	1563-1564
B5	18S	1731-1732	28S	2884-2885
B6	18S	1793	eL24	Arg 47
B7a	18S	970	28S	3710-3711 3742
B7b/c	Not observed			
B8	Not observed			
eB8	eS1	Glu 224 Leu 225	eL8	Glu 260 Lys 264
eB11	eS8	Arg 77 Asn 88 Glu 89 Arg 92 Asp105 Gln 167 Gly 169 Lys 170 Arg 200 Arg 205	28S	5026-5027 5024 2893-2894 3610-3611 3598-3599 5016-5017
eB12	18S	871 908-910 914	eL19	Arg 163 Arg 170 Arg 172 Arg 176
eB13	eS6	Ala 33 Thr 34 Arg131 Ile 141 Lys 143 Leu 144 Phe 145 Asn 146 Leu 147 Ser 148 Asp151 Gln 155 Tyr 156	eL24	Lys 69 Lys70 Arg71 Thr 72 Arg 73 Arg 74 Gln 79 Arg 80 Gly 84 Lys 93 Arg 94 Asn 95 Gln 96 Lys 97 Arg 101 Arg 105 Glu 106 Lys 117 Lys 124
	18S	1779-1781 1783 1746 1748-1750 323 327		
eB14	18S	1171-1175 1182-1183 1841-1847 1705-1706	eL41	Met 1 Arg 2 Lys 4 Arg 6 Arg 9 Arg 11 Lys 14 Arg 15 Arg 17 Arg 18 Arg 21

The contacting residues within 4 Å **radius** were selected using Contact (CCP4 suite of programs) and verified in the structure.